



Cite this: *Soft Matter*, 2024,  
20, 5221

## Structured bubbling in vibrated gas-fluidized beds of binary granular particles: experiments and simulations<sup>†</sup>

Jagan Mohan Sanghishetty,<sup>a</sup> Naimah M. Russ,<sup>c</sup> Christopher Spittler,<sup>a</sup> Qiang Guo,<sup>ID</sup><sup>a</sup> D. R. Nagaraj,<sup>b</sup> Raymond S. Farinato<sup>ID</sup><sup>b</sup> and Christopher M. Boyce<sup>ID</sup><sup>\*a</sup>

Mixing and segregation of granular particles on the basis of size and density from vertical vibration or upward gas flow is critical to a wide range of industrial, agricultural and natural processes. Recently, combined vibration and gas flow under certain conditions has been shown to create periodically repeating structured bubbling patterns within a fluidized bed of spherical, monodisperse particles. Here, we demonstrate with experiments and simulations that structured bubbling can form in binary mixtures of particles with different size and density, but with similar minimum fluidization velocities. Structured bubbling leads to particles mixing regardless of initial particle configuration, while exciting particles with only gas flow produces smaller unstructured bubbles which act to segregate particles. Discrete particle simulations match the experimental results qualitatively and, in some regards quantitatively, while continuum particle simulations do not predict mixing in the case of structured bubbling, highlighting areas for future model improvement.

Received 18th January 2024,  
Accepted 6th June 2024

DOI: 10.1039/d4sm00072b

rsc.li/soft-matter-journal

### 1. Introduction

Granular particles can be “fluidized” or excited into a fluid-like state by subjecting them to external forces which overcome gravitational force, typically either *via* vertical vibration<sup>1,2</sup> or vertical gas flow.<sup>3,4</sup> Gas flow fluidizes particles when the drag force overcomes gravity, given by the superficial gas velocity  $U$  being greater than  $U_{mf}$ , the minimum fluidization velocity.<sup>3</sup> Vertical vibration can bring grains into a fluid-like state when the peak vibrational acceleration is greater than gravitational acceleration, expressed non-dimensionally by the vibration strength:  $\Gamma = \frac{4\pi^2 f^2 A}{g} > 1$ , where  $f$  and  $A$  are the vibration frequency and amplitude, respectively, and  $g$  is the gravitational acceleration.<sup>5,6</sup> Combined gas flow and vibration in a vibrated gas-fluidized bed is often used to fluidize cohesive particles, and recent studies have demonstrated that combined gas flow and vibration can induce scalable, structured flow patterns in

grains,<sup>7</sup> such as structured bubbling,<sup>8</sup> convective cells<sup>9</sup> and surface waves.<sup>10</sup>

Mixing of particles of different size, density and shape is critical to a number of industrial and agricultural processes.<sup>11–18</sup> Fluidization of grains *via* vibration or gas flow can cause different types of grains to mix if vigorous convection is induced in the particles. However, vigorous fluidization of particles tends to be chaotic in nature,<sup>19,20</sup> making the dynamics difficult to scale and optimize, often causing granular flow processes operate inefficiently.<sup>21</sup> Less vigorous fluidization *via*  $\Gamma \sim 1$  or  $U/U_{mf} \sim 1$  often causes particles to segregate vertically on the basis of size or density.<sup>22–25</sup>

Gas voids or bubbles often rise through gas fluidized beds, inducing mixing mainly based on particles rising in the wake of bubbles.<sup>26</sup> The dynamics of these bubbles are typically mathematically chaotic;<sup>19</sup> however, oscillating gas flow<sup>19,20</sup> or combined constant gas flow and vibration<sup>8</sup> can structure bubbles to form and rise in a triangular array pattern. Structured bubbling has been demonstrated to form the same bubble patterns when scaled vertically<sup>27</sup> and horizontally<sup>8</sup> as well as create predictable particle convection patterns,<sup>28</sup> thus addressing issues with scale-up and optimization of fluidized bed processes.<sup>19</sup> So far, structured bubbling has only been demonstrated in monodisperse particles.

Here, we demonstrate that structured bubbling can form in binary mixtures of particles of different size and density subject to combined constant gas flow and vibration. Structured bubbling

<sup>a</sup> Department of Chemical Engineering, Columbia University, New York, NY 10027, USA. E-mail: [cmb2302@columbia.edu](mailto:cmb2302@columbia.edu)

<sup>b</sup> Department of Earth and Environmental Engineering, Columbia University, New York, NY 10027, USA

<sup>c</sup> Department of Chemical Engineering, Tuskegee University, Tuskegee, AL 36088, USA

† Electronic supplementary information (ESI) available. See DOI: <https://doi.org/10.1039/d4sm00072b>



causes the particles to mix, despite their differences in size and density. When subject to gas flow alone at the same velocity, the particles segregate with the denser particles falling to the bottom. Discrete particle and continuum particle simulations reproduce the structured bubbling in binary granular particles; however, while discrete particle simulations predict the particles mixing, continuum particle simulations predict the particles segregating.

## 2. Methods

### 2.1 Experiments

Transparent polymethyl methacrylate (PMMA) sheets were used to construct a pseudo-2D fluidized bed with 200 mm (width)  $\times$  8 mm (horizontal thickness)  $\times$  500 mm (height) dimensions. A 3 mm thick sintered bronze porous plate with an average pore size of 15  $\mu\text{m}$  (HENGKO Tech.) was used to support the particle bed and distribute gas flow uniformly across the base of the fluidized bed. The fluidized bed was mounted onto the top plate of an electrodynamic shaker (Labworks; ET-140), powered by its amplifier (Labworks Inc., FS-140) to induce vertical vibration. The instantaneous vibrational peak-to-peak displacement and frequency are measured and controlled using an accelerometer (PCB, J352C33), attached to the base of the bed. The shaker was operated and controlled using VibeLab software on a desktop computer. A schematic of the experimental setup is shown in Fig. 1.

Fluidizing air was fully humidified using a water bubbler to avoid static charge buildup. Antistatic liquid was sprayed on the internal surfaces of the bed as well as on the particles before they were poured into the bed. The top of the fluidized

bed was open to air at atmospheric pressure. All the particles that are used in the experiments are spherical in shape with property specifications as given in Table 1. The “light particles” had a density of  $\rho = 4100 \text{ kg m}^{-3}$  and a diameter of  $d_p = 400\text{--}600 \mu\text{m}$ , while the “heavy particles” had  $\rho = 6100 \text{ kg m}^{-3}$  and  $d_p = 400\text{--}500 \mu\text{m}$ . Both particle types had a minimum fluidization velocity  $U_{\text{mf}} = 0.37 \text{ m s}^{-1}$ . The bed was filled with particles to a total height of 50 mm. The minimum fluidization velocity for each of the components was determined experimentally, separately, by reducing the superficial gas velocity steadily with time with no vertical vibration applied, from a vigorously bubbling state until no bubbles and no particle motion were observed. In these de-fluidization experiments, the pressure drop across the bed was monitored using a LabVIEW program. The value of  $U_{\text{mf}}$  was determined as the highest superficial velocity at which the pressure drop across the bed was below the value needed to support the weight of the bed per unit cross-sectional area. For bubbling fluidization experiments, the gas flow rate was kept at a constant value, corresponding to  $U/U_{\text{mf}} = 1.4$ . A mass flow controller (Alicat; MCP-250 slpm), was used to control the gas flow rate. These gas flow and vibration conditions were chosen because they have been shown previously in monodisperse particles<sup>8</sup> to create the highest level of structured bubbling, and the level of structuring decreases significantly with minor changes in gas flow and vibration conditions. We only use these gas flow conditions with and without vibration so as to compare highly structured bubbling with unstructured bubbling directly. We leave it to future studies to compare across a range of vibration and gas flow conditions to study the effects of partial bubble structuring on binary particle mixtures.

Optical imaging and high-speed videos of the front view of the bed were captured using an advanced color camera (AOS Technologies AG, PROMON U750) at a framerate of 50 frames per second, corresponding to ten times the vibration frequency of the shaker. The experiments were carried out over the course of 180 s. A red colored non-reflecting background was used in optical imaging to aid the particle tracking to provide color contrast with particles. The white-colored light particles and black-colored heavy particles contrasted with the red background. Five different initial conditions or particle arrangements are used in the experiments to study the mixing and segregation characteristics as shown in Fig. 2. In binary configurations, equal bulk volumes of both types of particles were added. The bottom 12 mm of particles of the bed cannot be observed as they are blocked by the horizontal opaque acrylic plate that joins fluidized bed to the gas distributor. Thus, the bottom layer of particles appears to be shorter than the top layer in experiments, although the two layers in fact are equal in height.

The gas flow rate for all the experiments was kept at  $1.4U_{\text{mf}}$  along with vibration conditions of  $f = 5 \text{ Hz}$  and  $A = 4.5 \text{ mm}$ , corresponding to a vibration strength of  $\Gamma = 0.45$ . These gas flow and vibration conditions were chosen because prior experimental results indicated that they produced the most structured or patterned bubbling for a range of monodisperse

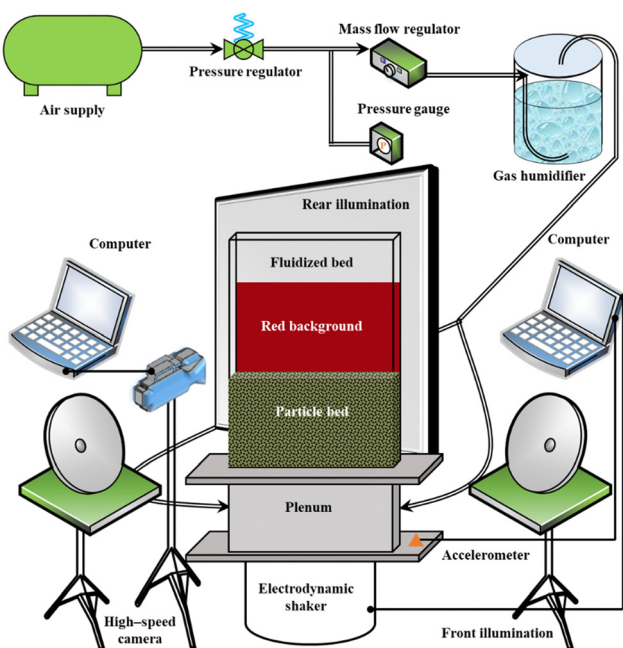


Fig. 1 Schematic of the experimental setup showing the gas flow line, various instrumentation and the fluidized bed with a red background mounted on a shaker with both front and rear lighting arrangements.



Table 1 Particle properties used in the experiments and simulations

Method	Component	Size range ( $\mu\text{m}$ )	Material density ( $\text{kg m}^{-3}$ )	Material	$U_{\text{mf}}$ ( $\text{m s}^{-1}$ )	Color
Experiment	Light	400–600	4100	Ceramic	0.368	White
Experiment	Heavy	400–500	6100	Ceramic	0.372	Black
CFD-DEM	Light	500	4000	Ceramic	0.332	White
CFD-DEM	Heavy	415	6000	Ceramic	0.332	Black
MFM	Light	500	4000	Ceramic	0.284	White
MFM	Heavy	415	6000	Ceramic	0.293	Black

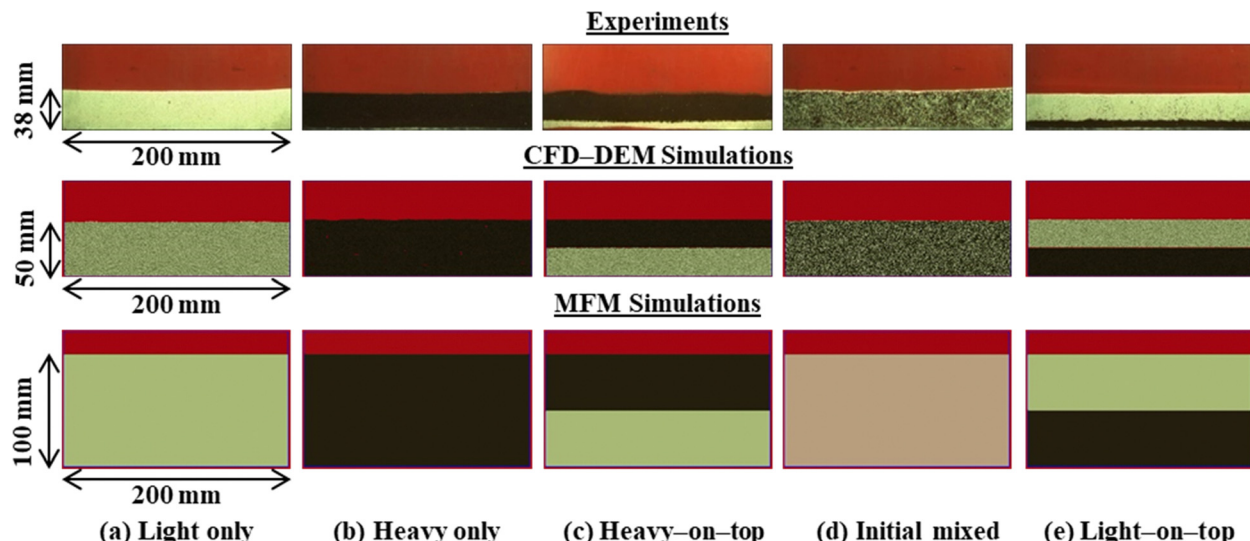


Fig. 2 Optical images of different initial conditions (a)–(e) that are used in experiments, CFD-DEM simulations and MFM simulations. In experiments, the initial fill height of particles is 50 mm, but the bottom 12 mm of particles of the bed cannot be observed due to a horizontal plate that joins the fluidized bed to the gas distributor.

particles.<sup>8</sup> Gas flow and vibration were induced simultaneously to start the experiment. Front-lighting was used to quantify the mixing characteristics of the system. After recording the front-lighting case for 180 s, the system was switched to backlighting while keeping the gas flow and vibration in progress. A backlighting video was recorded to image bubble dynamics after a statistical-steady-state had been reached.

## 2.2 CFD-DEM simulations

Computational fluid dynamics-discrete element method (CFD-DEM)<sup>29</sup> simulations were used to model the coupled gas-granular flow. This method models the interstitial gas as a continuum using CFD and tracks the particles using DEM.<sup>30</sup> In CFD-DEM, the CFD cells are larger than the particles, and gas flow is solved for using volume-averaged Navier-Stokes equations<sup>31</sup> accounting for the gas volume fraction of each cell. Particle motion is tracked using Newtonian kinematics with contact forces accounted for based on springs and dashpots for the overlap between “soft” spheres. Particle and gas flow are coupled based on buoyancy and a drag law<sup>32</sup> based on the particle Reynolds number and local particle volume fraction. CFDEMcoupling open-source software was used for these simulations; this software couples the CFD of OpenFOAM with

the DEM of LIGGGHTS. The full CFD-DEM model equations are provided in the ESI.†

**2.2.1 CFD-DEM simulation setup.** To match the experimental conditions, in a computational bed of same width (200 mm), a particle bed height of 50 mm was initialized for both monodisperse and binary setups. For binary configurations, bulk volumes of both particle types were equal, as seen in Fig. 2. Particle size and density were very similar to those in experiments, as shown in Table 1. The horizontal depth of the pseudo-2D computational bed was 4.0 mm, which is equivalent to two cell widths, and each cell width was 4 to 5 particle diameters, following recommendations from grid sensitivity studies in the literature.<sup>33</sup> This horizontal depth was smaller than the 8 mm used experimentally in order to save computational expense. The computational domain height is 200 mm, shorter than the 500 mm used experimentally, to accommodate bubbling, bed expansion and a freeboard to avoid loss of the particle-phase. This shorter computational height was used to save computational expense. The air had a kinematic viscosity of 18  $\mu\text{Pa s}$  and a density of 1.2  $\text{kg m}^{-3}$ . The CFD mesh was uniform throughout the domain with the size of 2.0 mm in all the directions. For the gas phase, periodic boundaries were specified for the side walls with front and back walls modelled as no-slip walls. For the solids phase, the side walls were

modelled as periodic whereas the front and back walls were modelled as inelastic flat walls. A spatially uniform mass inflow boundary was specified for the bottom wall to replicate airflow from the distributor in experiments and a spatially uniform pressure outflow boundary was specified for the top of the system. Vibration of the system was modeled by sinusoidal variation of the gravity force vector along the vertical vibration direction, given by

$$g = 9.81 + (2\pi f)^2 A \sin(2\pi f t) \quad (1)$$

Here,  $t$  is the time coordinate.  $A$  and  $f$  were 4.5 mm and 5.0 Hz, respectively. It is important to note that frequency and amplitude in CFDEM simulations are same as in experiments. A constant superficial gas velocity of  $1.4U_{\text{mf}}$ , matching experiments, was set as inlet boundary condition. The same initial particle arrangements are used in simulations and experiments, as shown in Fig. 2.

### 2.3 MFM simulations

Multi-fluid model (MFM) Simulations were carried out using MFix,<sup>34</sup> an open-source software package created by the National Energy Technology Lab for modelling multiphase gas-granular flows. The solid particles are approximated to be a continuous medium, interpenetrating with fluidizing gas and other solids species within a Eulerian grid. This simulation method is advantageous over methods, such as CFD-DEM, that resolve individual particles, as it is much less computationally intensive and capable of simulating larger systems. Behavior of the fluidized solids are modelled according to the kinetic theory of granular flows (KGTF)<sup>35</sup> combined with frictional solids stress models from soil mechanics for high particle volume fractions.<sup>36</sup> Conservation of momentum for each solid species is solved for and coupled to the gas momentum equation *via* a drag law, in this case the Gidaspow drag model.<sup>37</sup> The overall particle rheology was simulated using the Guo-Boyce model.<sup>8</sup> Further, a momentum exchange model between the two solids phases was used.<sup>38</sup> The full MFM model equations are provided in the ESI.<sup>†</sup>

**2.3.1 MFM simulation setup.** The MFM simulation setup was identical in overall size, grid size and boundary conditions to the CFD-DEM simulations, except the fill height of particles and the overall system height were twice as high (Fig. 2). The fill height of particles was made twice as high, since this height was needed for structured bubbling to form. For both gas and solid phases, periodic boundaries were specified for the side walls. Front and back walls were modelled as no-slip walls for the gas phase and partial slip walls using the Johnson-Jackson boundary condition<sup>39</sup> for the solids phases. Vibration was also modeled by vibrating gravity. A gas inlet velocity of  $1.4U_{\text{mf}}$  and vibration frequency of 5 Hz were used in MFM simulations, matching CFD-DEM simulations and experiments. The vibration amplitude was 6.0 mm, higher than the 4.5 mm used in CFD-DEM simulations and experiments, since this vibration amplitude was needed to produce structured bubbling in MFM simulations. The same initial configurations of particles were used as in experiments and CFD-DEM simulations (Fig. 2),

except the overall height of particles was twice as high. The particle properties and  $U_{\text{mf}}$  values are given in Table 1.

### 2.4 Post-processing

**2.4.1 Correlation coefficient.** In experiments and CFD-DEM simulations, Pearson's correlation coefficient<sup>40</sup> was used to quantify the level of repetition of bubble structuring. The time interval across images compared was 0.4 s, or two vibration periods, whether vibration was used or not in the simulation or experiment. The correlation coefficient was averaged over the course of the simulation or experiment after statistical steady state was achieved. The correlation coefficient is given by:

$$r = \frac{\sum_{i=1}^N (G'_i - \bar{G}')(G_i - \bar{G})}{\sqrt{\sum_{i=1}^N (G'_i - \bar{G}')^2 \sum_{i=1}^N (G_i - \bar{G})^2}}, \quad (2)$$

The correlation coefficient,  $r$ , has a value of 1 if two images are exactly the same and a value of 0 if the two images are exactly inverted. Here,  $N$  is the number of pixels, and  $G_i$  and  $G'_i$  are the intensity at pixel  $i$  in one frame and a frame two vibration periods later, respectively. Overbars indicate averages over space and time after statistical steady state has been reached. For experiments, the  $G$  values are taken based on the grayscale value of signal intensity in backlit images with pixels gathered together into square groups 4.0 mm in side length to match the size of CFD cells in simulations. In CFD-DEM, the  $G$  values are taken based on the void fraction in the CFD cells.

**2.4.2 Mixing index.** In experiments and CFD-DEM simulations, the normalized mixing entropy index<sup>41</sup> was used to quantify the level of mixing over time. Mixing entropy was calculated by first dividing the system into cells and counting the number of each particle type per cell. The cell mixing entropy  $s(k)$  was then calculated using:

$$s(k) = x_1(k) \ln x_1(k) + x_2(k) \ln x_2(k) \quad (3)$$

with  $x_1(k)$  being the number of particles of type 1 in cell  $k$  divided by the total number of particles in cell  $k$ . The number of particles in CFD-DEM is characterized by directly counting the number of particles in 4 mm square cells (the CFD cell size), and the number of pixels that were yellow or black in experiments was used to estimate the ratio of number of particles in cell sizes of the same size in experimental image analysis. The average of the entropy values of all the cells is taken, weighted by the total number of particles in each cell, giving a value for the entropy of the entire system at time  $t$ :

$$\text{ME}(t) = \frac{1}{N} \sum_k n(k, t) s(k, t) \quad (4)$$

where  $n(k, t)$  is the total number of particles in cell  $k$  and  $N$  is the total number of particles in the system.  $\text{ME}(t)$  is then normalized to a value between 0 and 1, where 0 corresponds to a fully



segregated system and 1 corresponds to a fully mixed system.

$$ME_n(t) = \frac{ME(t) - ME_{seg}}{ME_{mix} - ME_{seg}} \quad (5)$$

where  $ME_{mix}$  and  $ME_{seg}$  are found by performing the ME calculation from eqn (4) on frames of a fully mixed and fully segregated system.

### 3. Results and discussion

#### 3.1 Flow dynamics

Experiments, CFD-DEM simulations and MFM simulations demonstrate flow dynamics in binary mixtures of particles with (i) different initial particle configurations and (ii) gas flow alone *vs.* combined gas flow and vibration to investigate the effects of these parameters on bubble dynamics and particle mixing.

**3.1.1 Experiments.** Experiments using combined gas flow and vibration show that structured bubbling patterns form the same triangular bubbling patterns regardless of the initial particle configuration with the bubble pattern repeating every two vibration periods (Fig. 3). Once a statistical steady state is achieved, the particles are fairly well mixed throughout the bubbling pattern repetition, with a slight tendency for light particles to be on top and heavy particles to be on bottom, regardless of the initial particle configuration (Fig. 4c–e). The structured bubbling patterns form whether there is only one particle type (Fig. 4a and b) or two particle types in a fairly well-mixed state (Fig. 4c–e). Particles mix faster from structured bubbling when heavy particles are on top as compared to when light particles are on top (Fig. 5), which can be attributed to bubbles carrying light particles up in bubble wakes faster than lifting heavy particles.

Experiments with only gas flow through particles show that gas bubbles smaller than those seen in the vibration cases

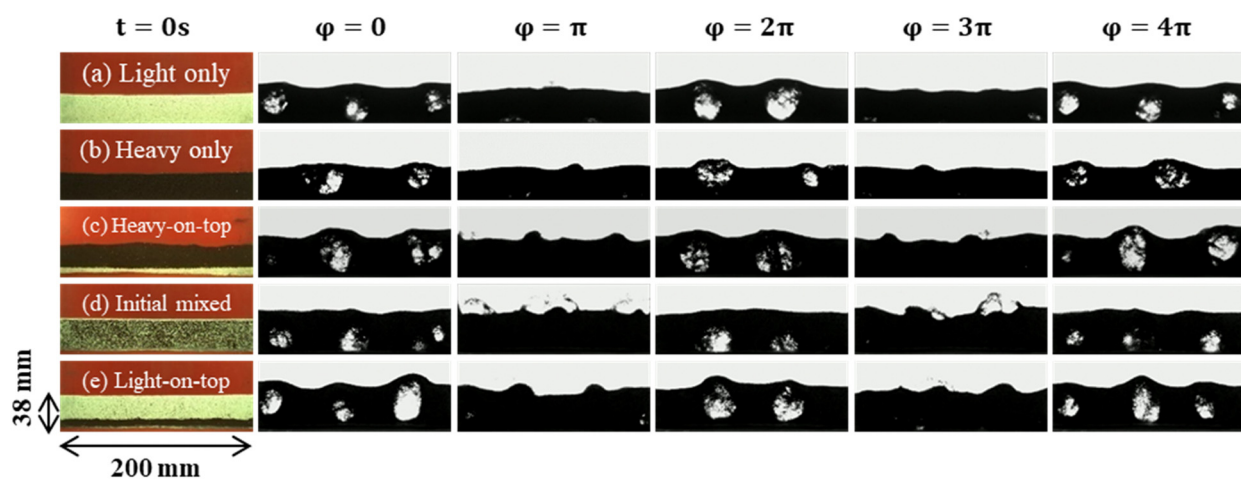


Fig. 3 Time series of backlit images of experimental cases with combined gas flow and vibration over the course of two vibration periods after statistical steady-state is reached for different initial particle configurations (a)–(e).

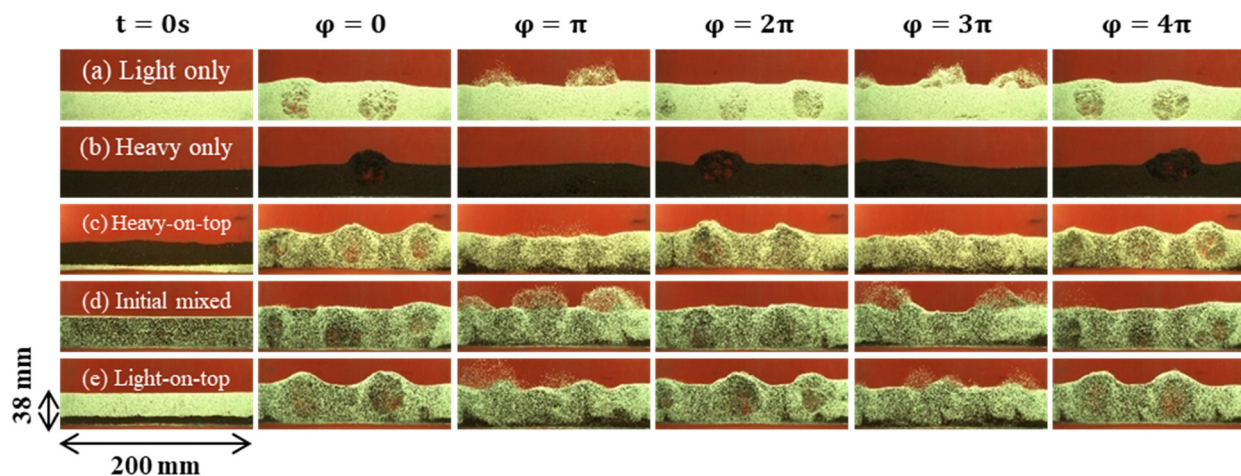


Fig. 4 Time series of front-lit images of experimental cases with combined gas flow and vibration over the course of two vibration periods after statistical steady state is reached for different initial particle configurations (a)–(e).

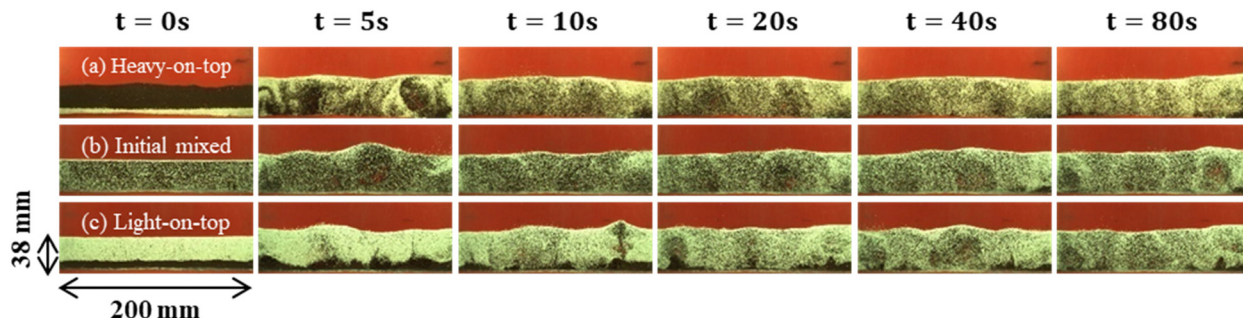


Fig. 5 Time series of front-lit images of experimental cases with combined gas flow and vibration for different initial configurations (a)–(c).

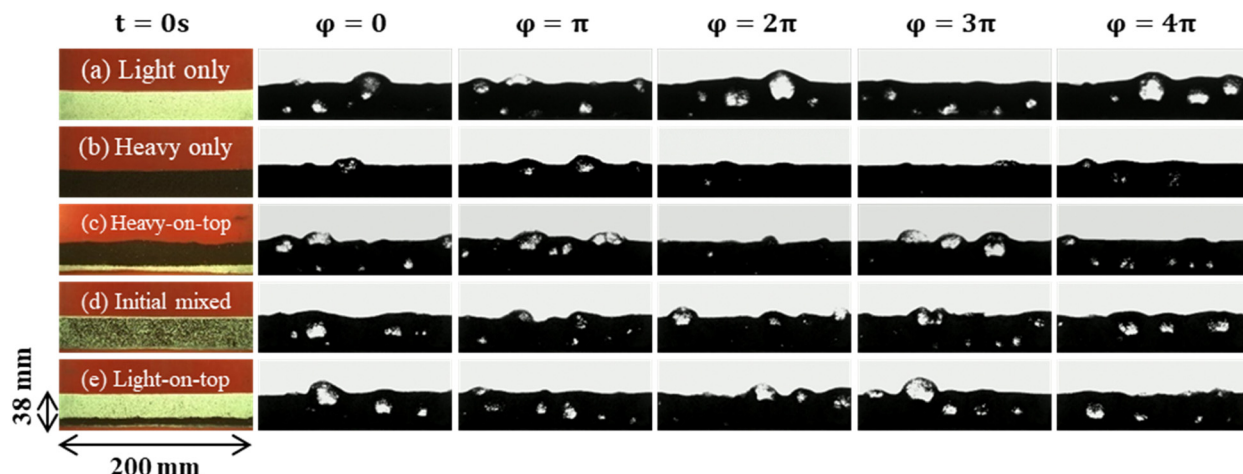


Fig. 6 Time series of backlit images of experimental cases with only gas flow over the equivalent duration of two vibration periods after statistical steady-state is reached for different initial particle configurations (a)–(e).

rise in a disordered manner through the particles, regardless of the initial particle condition (Fig. 6). At steady-state in binary mixture cases, particles are somewhat mixed, yet heavy particles tend to gather at the bottom of the bed and light particles tend to gather at the top of the bed throughout the

bubble dynamics (Fig. 7). From the start of the experiments, if heavy particles are on bottom, the heavy particles stay on bottom, but if heavy particles are on top, heavy particles migrate to the bottom over the course of the experiment (Fig. 8). Heavy particles migrate to the bottom faster if heavy

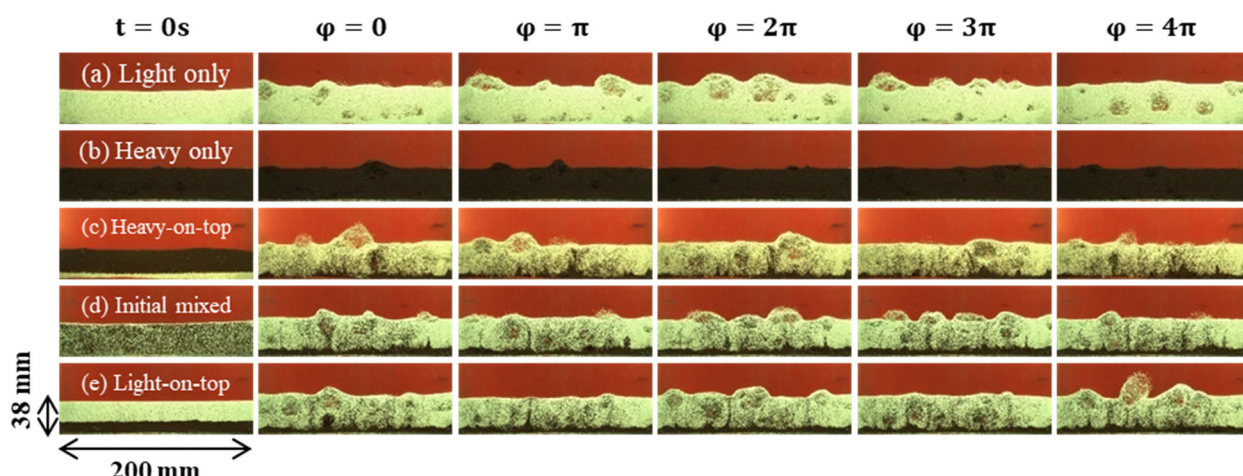


Fig. 7 Time series of front-lit images of experimental cases with only gas flow over the equivalent duration of two vibration periods after statistical steady state is reached for different initial particle configurations (a)–(e).



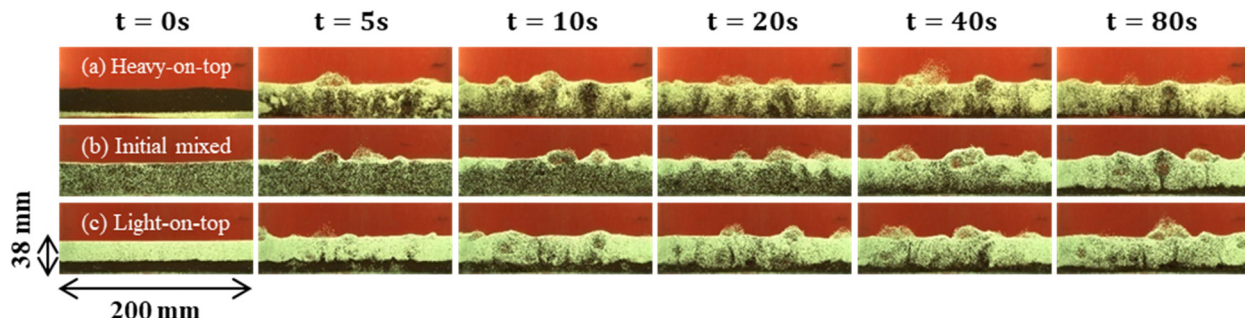


Fig. 8 Time series of front-lit images of experimental cases with only gas flow for different initial particle configurations (a)–(c).

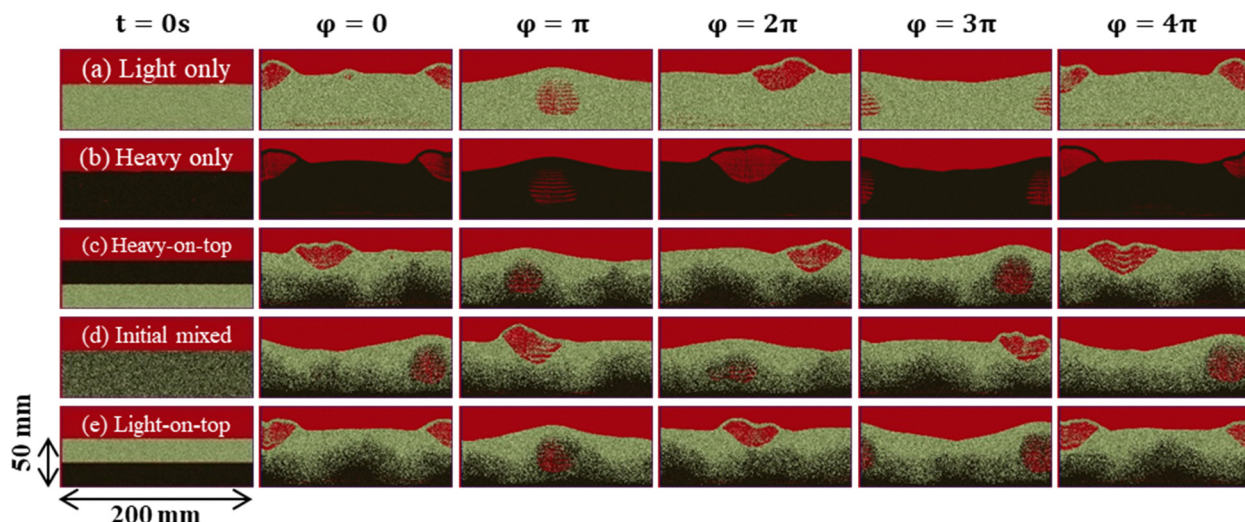


Fig. 9 Time series of images of CFD-DEM simulations with combined gas flow and vibration over the course of two vibration periods after statistical steady-state is reached for different initial particle configurations (a)–(e).

particles are on top in the initial configuration as compared to an initially mixed configuration (Fig. 8).

**3.1.2 CFD-DEM simulations.** CFD-DEM simulations of combined gas flow and vibration show that an alternating structured bubbling pattern which repeats itself every two vibration cycles occurs in monodisperse particles as well as binary particle mixtures of different configurations (Fig. 9). Once statistical steady state is achieved in binary mixtures,

the particles are fairly well mixed, yet heavy particles tend to migrate toward the bottom and light particles tend to migrate toward the top, regardless of the initial particle configuration (Fig. 9c–e). Particles stay fairly well mixed over time if they are initially mixed, and the particles mix faster if the light particles are at the bottom than if the heavy particles are at the bottom (Fig. 10). These results match qualitatively with those observed experimentally.

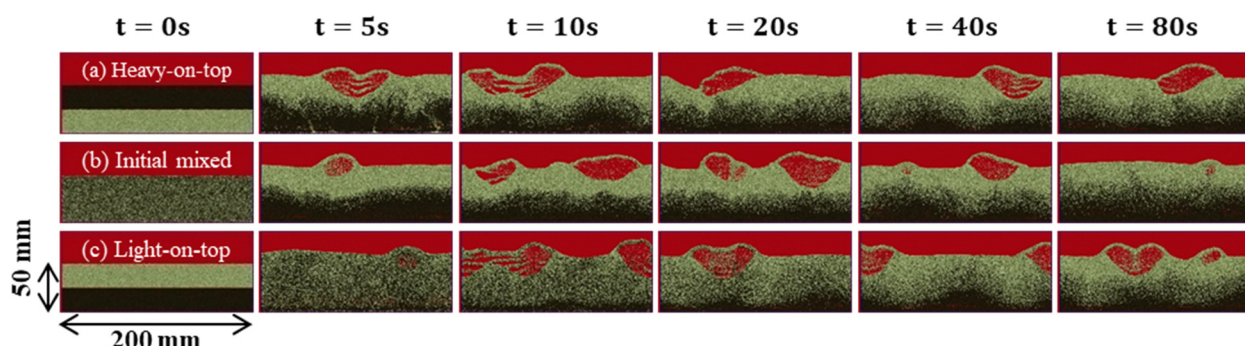
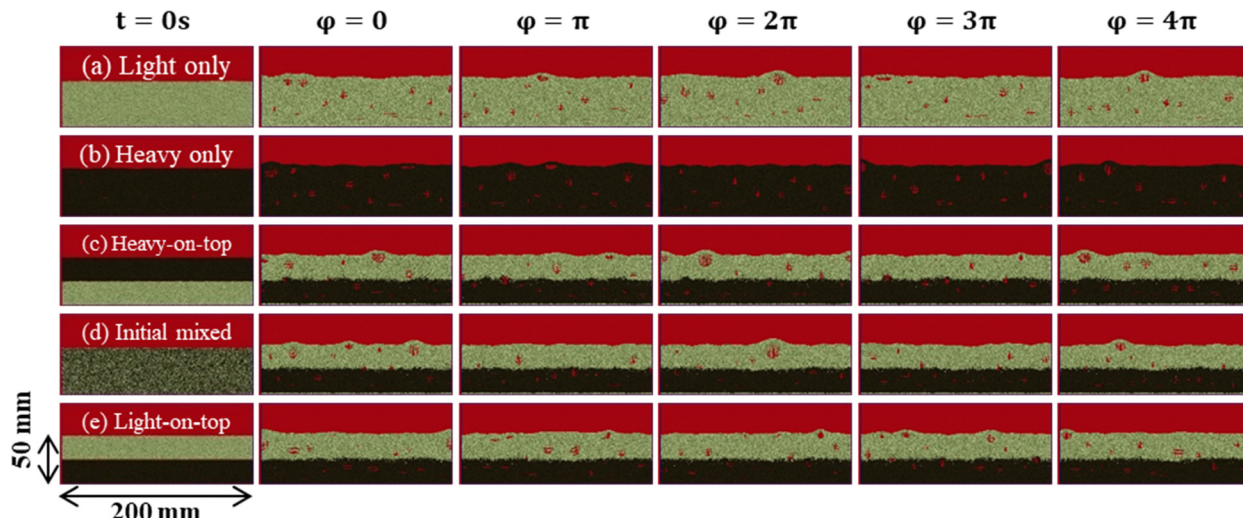


Fig. 10 Time series of images of CFD-DEM simulations with combined gas flow and vibration for different initial particle configurations (a)–(c).





**Fig. 11** Time series of images of CFD-DEM simulations with only gas flow over the equivalent duration of two vibration periods after statistical steady-state is reached for (a) light particles only, (b) heavy particles only, and (c)–(e) binary mixtures with (c) light particles on the top, (d) particles initially mixed and (e) light particles on the bottom.

When no vibration is used in CFD-DEM simulations (Fig. 11), bubbles are smaller than those under vibration conditions, regardless of initial particle configuration, matching experimental results qualitatively. Further, in binary particle mixtures heavy particles migrate to the bottom once statistical steady state is achieved throughout the bubble rise process, regardless of initial particle configuration (Fig. 11), matching experimental results qualitatively. Over time, particles segregate in binary mixtures (Fig. 12), and particles segregate faster if light particles are on top than if particles are initially mixed, matching experimental results qualitatively. Particle segregation is more complete in CFD-DEM simulations than that observed in experiments.

**3.1.3 MFM simulations.** Multi-fluid model (MFM) simulations were conducted for comparison with the experiments and CFD-DEM simulations. When the same 5 cm total bed height is used in the simulations, no structured bubbling is seen, and thus we increase the total bed height to 10 cm in which the bubbles have space to evolve to form structured bubbling patterns. With combined gas flow and vibration, structured bubbling with a triangular bubble pattern and a repetition time of two vibration periods is seen, matching experimental results

qualitatively (Fig. 13). However, particles fully segregate over time with light particles going to the top in MFM simulations (Fig. 13 and 14), not matching the mixing observed experimentally. When no gas flow is used, smaller bubbles form in MFM simulations, with no apparent structuring (Fig. 15), matching experimental results qualitatively. Particles segregate over time (Fig. 16) with lighter particles rising to the top, matching experimental results qualitatively, although the rate of segregation is much faster than that observed experimentally. The requirement of a taller bed height to achieve structured bubbling and the prediction of particles segregating rather than mixing under structured bubbling demonstrate significant inaccuracies in MFM predictions of the dynamics of structured bubbling in binary particle mixtures.

### 3.2 Structured bubbling quantification

Pearson's correlation coefficient is used to quantify the amount of structuring in the bubbles for the experimental and CFD-DEM cases with and without vibration once statistical steady-state is achieved (Fig. 17). Experiments, CFD-DEM and MFM simulations all show that cases with vibration have significantly

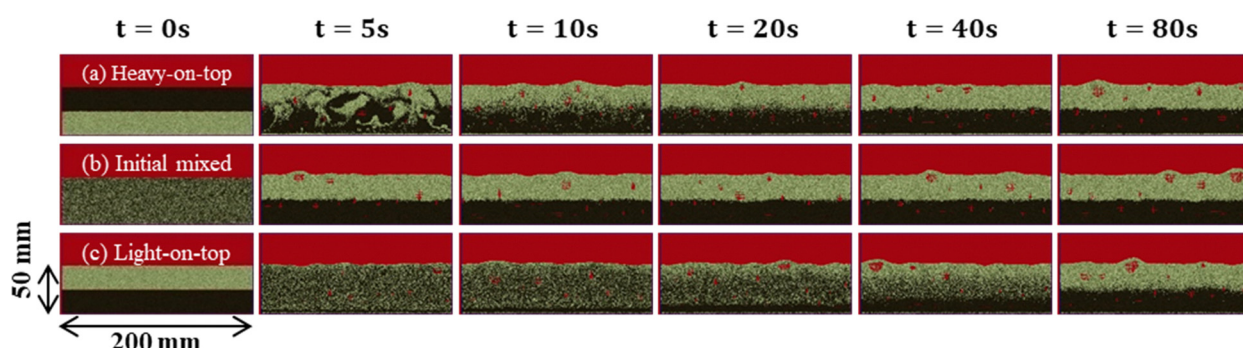


**Fig. 12** Time series of images of CFD-DEM simulations with only gas flow for different initial particle configurations (a)–(c).



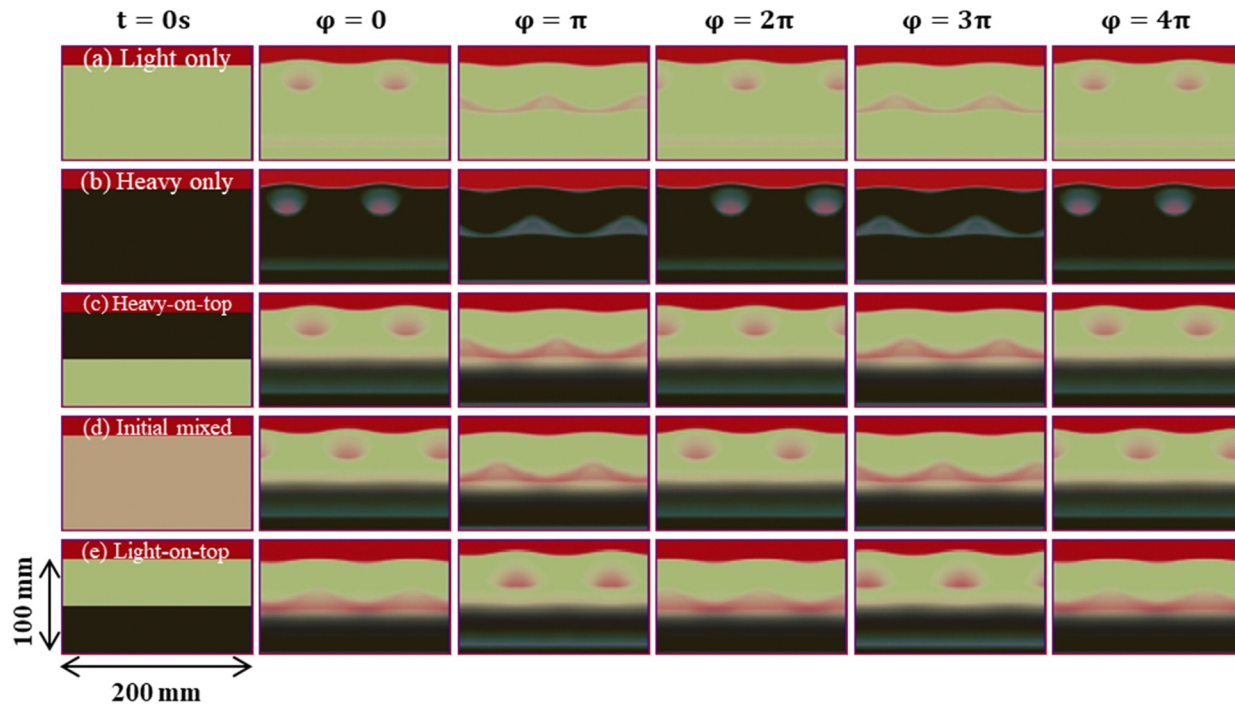


Fig. 13 Time series of images of MFM simulations with combined gas flow and vibration over the course of two vibration periods after statistical steady state is reached for different initial particle configurations (a)–(e).

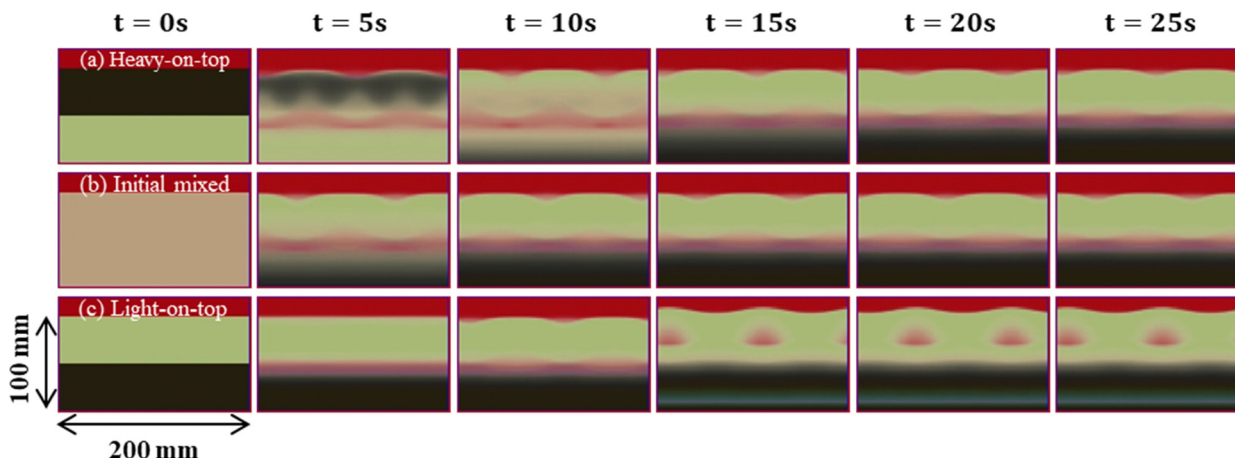


Fig. 14 Time series of images of MFM simulations with combined gas flow and vibration for different initial particle configurations (a)–(c).

higher bubble structuring than cases without vibration, and there is no significant difference in correlation coefficient in vibration cases with varying initial conditions. CFD-DEM simulations match experimental results quantitatively accurately with vibration, but CFD-DEM simulations without vibration have higher correlation coefficients than experiments, possibly due to the fact that a sintered bronze porous plate was used as distributor in experiments, while a uniform gas flow was induced from the bottom in simulations. MFM simulations predict correlation coefficients significantly higher than those in all experimental cases, essentially 1.0 in vibrated cases, as well as smaller standard deviations in correlation coefficients,

indicating MFM simulations fail to capture the disordered dynamics of fluidization.

### 3.3 Mixing quantification

The amount of mixing over time in experiments as well as CFD-DEM and MFM simulations with and without vibration and with different initial configurations is quantified using the mixing entropy (Fig. 18). Experimental and CFD-DEM cases show that particles are well-mixed when vibration is used (as shown by a steady-state value above 0.5), but well-segregated when no vibration is used (as shown by a value below 0.5). Rates of particle mixing in CFD-DEM simulations match experiments

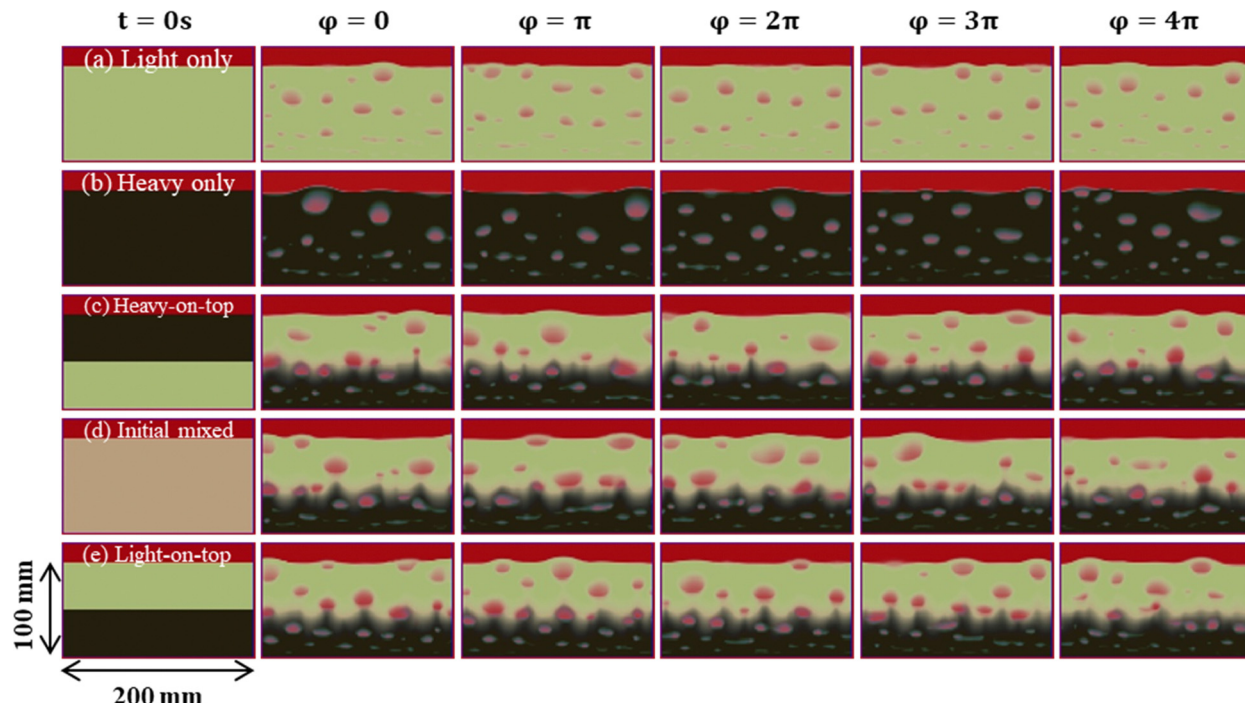


Fig. 15 Time series of images of MFM simulations with only gas flow over the equivalent duration of two vibration periods after statistical steady state is reached for different initial particle configurations (a)–(e).

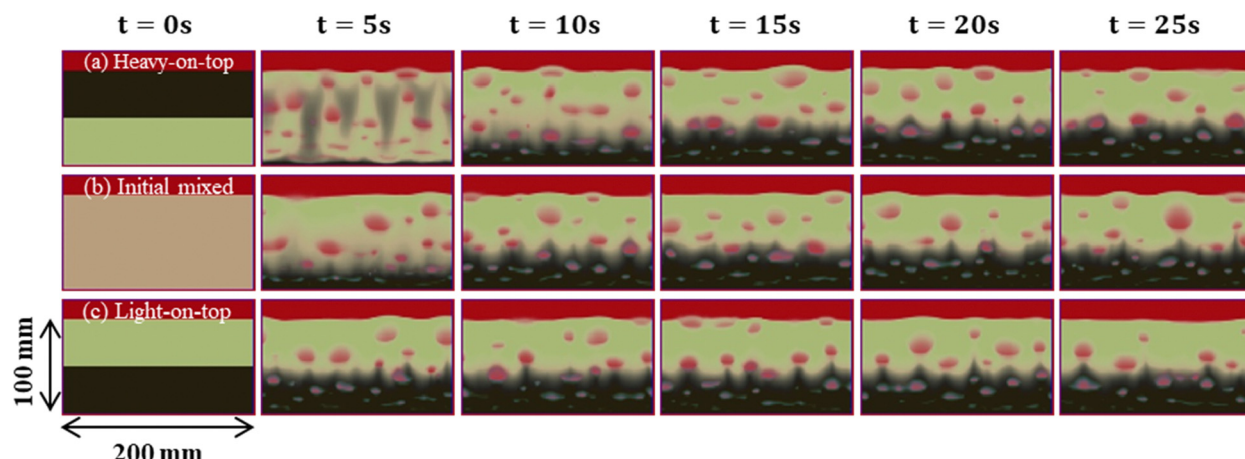


Fig. 16 Time series of images of MFM simulations with only gas flow for different initial particle configurations (a)–(c).

fairly well for the vibration cases, yet at steady state, CFD-DEM simulations predict more segregation in cases without vibration than observed experimentally. In contrast, MFM simulations predict the same low levels of mixing whether or not vibration is used, missing the key experimental insight that vibration promotes mixing. The amount of segregation predicted by MFM for the no vibration case matches experiments more closely than that of CFD-DEM, but the MFM simulations are still qualitatively inaccurate in that MFM predicts the same level of segregation with and without vibration.

**3.3.1 Discussion of the mechanisms for structured bubbling and mixing.** We investigate how vibration induces structured

bubbling in binary particle mixtures by examining the CFD-DEM and MFM simulation predictions in more depth. Fig. 19 shows the (a) particle positions, (b) particle packing fraction and particle convection patterns and (c) particle positions at points in time just before bubbles form in CFD-DEM simulations with vibration. For this structured bubbling case, at  $\varphi = 0$  in the vibration cycle (i), particles are tightly packed both below the bubble and to the side of the bubble, creating a solid-like state characterized by high particle pressures due to strong particle contacts. This solid-like state prohibits bubbles forming at this point in time, explaining the formation of bubbles in rows at specific points in time. At  $\varphi = \pi/5$  (ii), fast particle



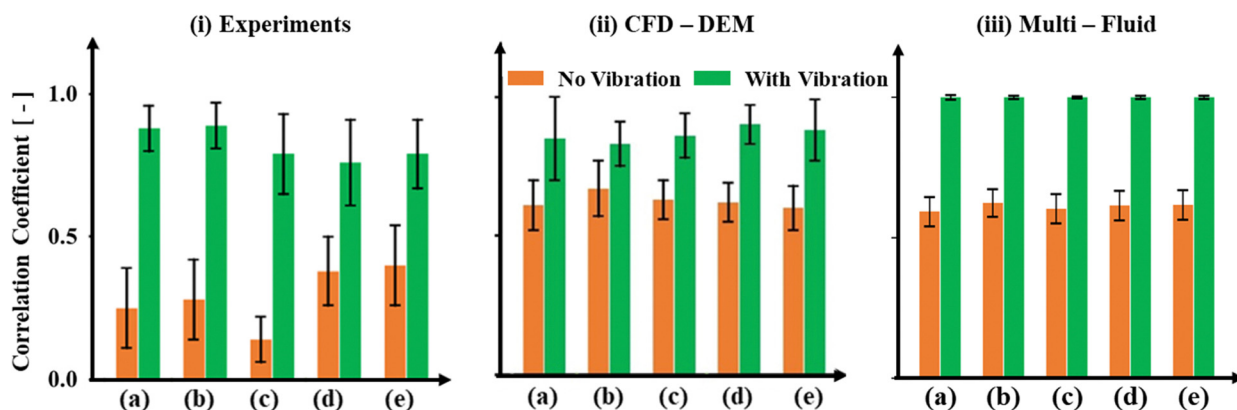


Fig. 17 Bar graphs of correlation coefficient for experiments and CFD-DEM and MFM simulations with and without vibration after statistical steady state is achieved for different initial particle configurations: (a) light particles only, (b) heavy particles only and (c) heavy particles on top, (d) particles initially mixed and (e) light particles on top. Error bars show the standard deviation over the course of the time frames in the experiment or simulation.

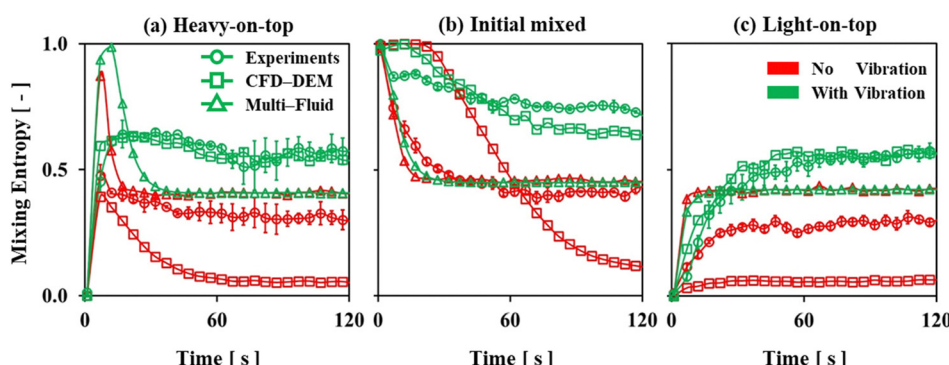


Fig. 18 Mixing entropy vs. time for experiments (with error bars for standard deviation between 3 experiments) and CFD-DEM and MFM simulations (without error bars) for different initial particle configurations (a)–(c).

convection patterns around the bubble lead to a solid-like state directly below the bubble with a high packing fraction and high particle pressure, but a fluid-like state with lower packing fraction and particle pressure below and to the side of the bubble. As such, a new row of bubbles is able to form below and to the side of the bubble seen in Fig. 19 (ii) at this time, explaining the formation of rows and a triangular pattern for the bubble formation. Since bubbles can only form at certain points in time and certain locations, there is a large amount of gas that can channel to these bubbles, explaining the large bubbles formed. This mechanism is consistent with that described previously for monodisperse particles,<sup>8</sup> despite the fact that a mixture of particles is observed surrounding the bubble (Fig. 19(a)).

Fig. 20 is equivalent to Fig. 19, but Fig. 20 shows the CFD-DEM case without vibration. Particle convection patterns are much slower around bubbles (as seen from much smaller green arrows), and thus there are no solid-like regions surrounding bubbles, as demonstrated by lower particle packing fractions and particle pressures. As such, with fluid-like regions everywhere in the system at all times, bubbles can form at any time and any place at the distributor and bubbles form randomly. Since bubbles are forming at all times, there is not as much gas

to channel to bubbles when they form, and bubbles are smaller than in the case with vibration and more bubbles are formed (Fig. 20). Thus, the formation of solid-like regions in the case with vibration and the lack of solid-like regions in the case without vibration explains the difference in bubble dynamics between these two cases.

MFM simulations with vibration (Fig. 21) show that particle convection patterns around bubbles lead to solid-like regions preventing bubble formation both directly below bubbles and to the side of bubbles at  $\varphi = 0$  in the vibration cycle (i). Particle convection patterns then lead to a fluid-like region forming below and in-between bubbles at  $\varphi = \pi/6$  (ii), explaining the formation of a new bubble in this region and a triangular bubble pattern. However, due to the formation of a broad pocket of gas low in the bed, the switching between solid-like and fluid-like behavior only forms roughly halfway through the bed vertically, and thus structured bubbling only forms in the upper half of the bed. Thus, the difference in the vertical location of switching solid-like and fluid-like regions in CFD-DEM simulations and MFM simulations with vibrations explains the difference in the structured bubbling patterns formed.

MFM simulations without vibration (Fig. 22) show that particle convection patterns lead to some areas of high packing

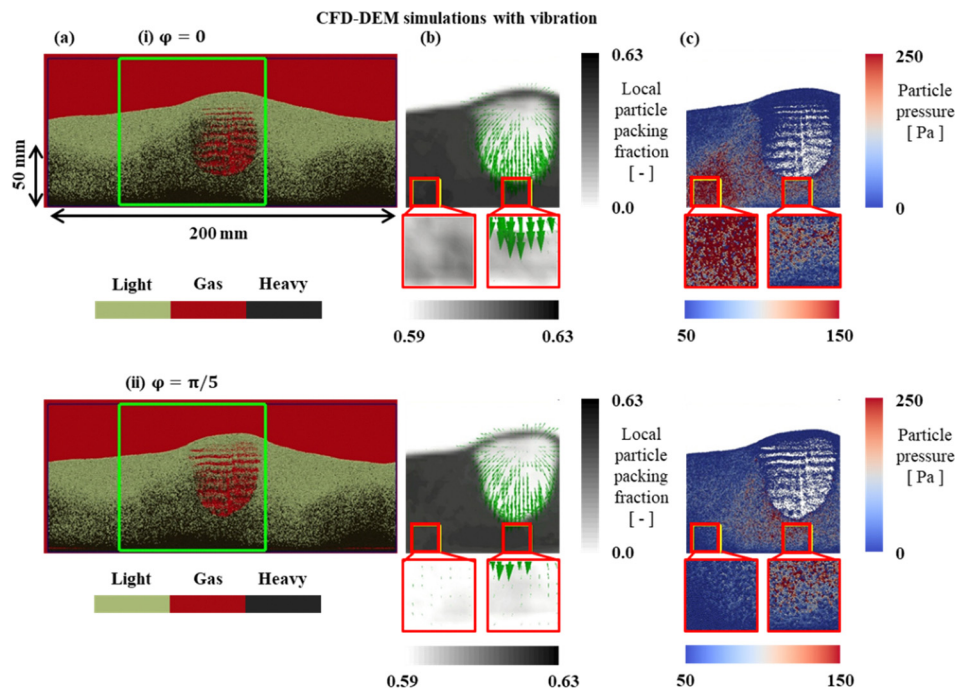


Fig. 19 (a) Heavy and light particle positions, (b) particle packing fraction and particle convection pattern and (c) particle pressure at two points in the vibration cycle in CFD-DEM simulations with vibration.

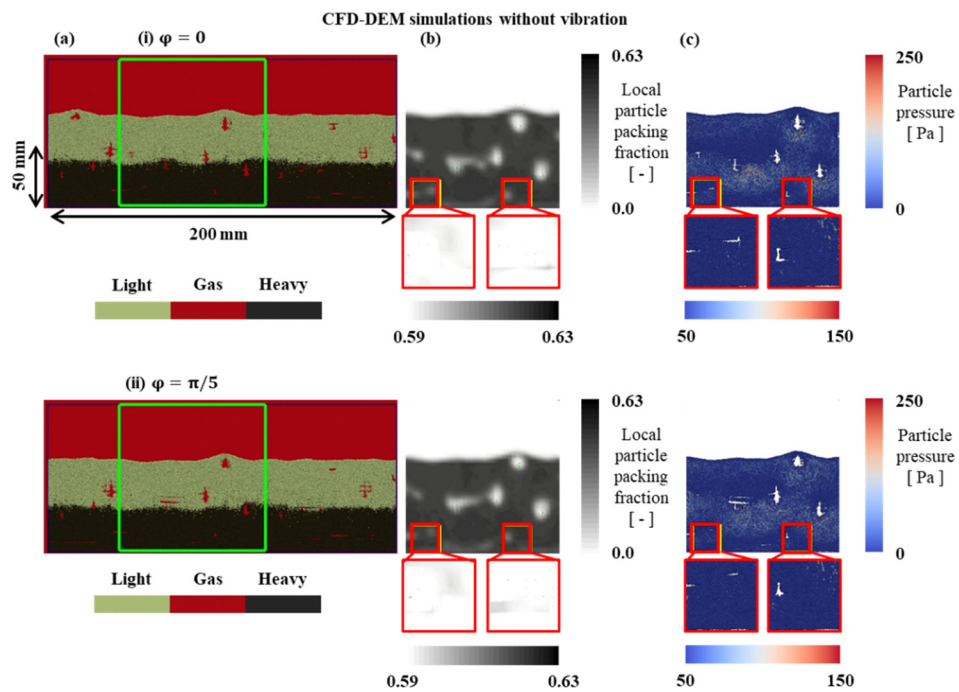


Fig. 20 (a) Heavy and light particle positions, (b) particle packing fraction and particle convection pattern and (c) particle pressure at two points in the vibration cycle in CFD-DEM simulations without vibration.

fraction and particle pressure below bubbles, but there is no pattern of when and where these regions form, and thus no structured bubbling pattern forms. These results from MFM are somewhat different from those in CFD-DEM (Fig. 20) in

which no solid-like regions form, but due to a lack of temporal and spatial formation of solid-like regions, both simulation techniques predict random bubble dynamics, matching experiments.



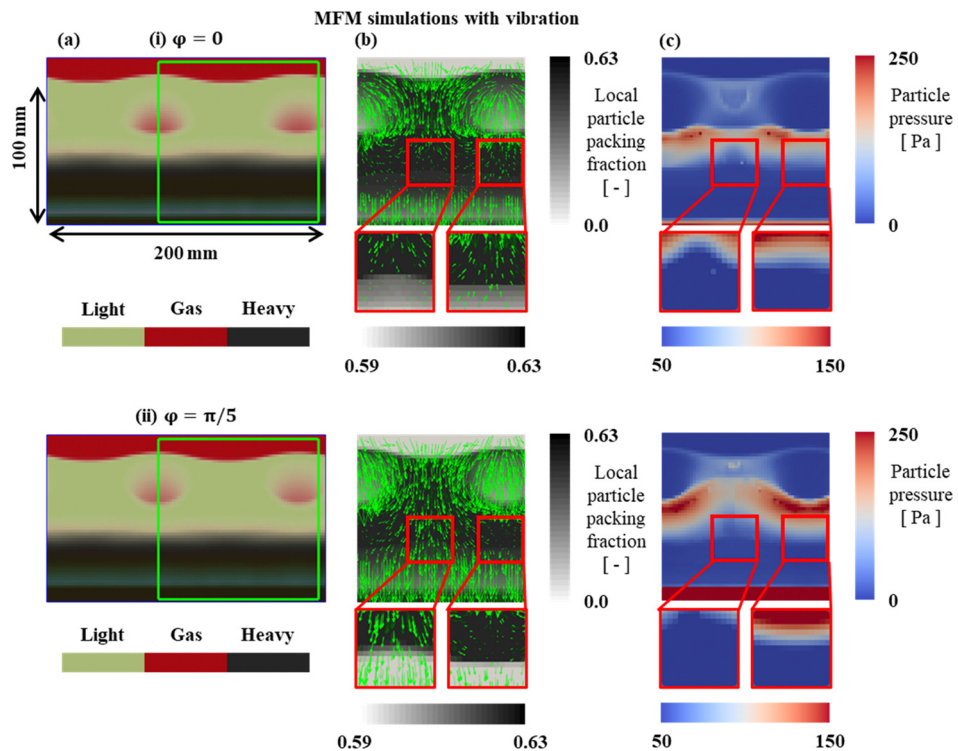


Fig. 21 (a) Heavy and light particle positions, (b) particle packing fraction and particle convection pattern and (c) particle pressure at two points in the vibration cycle in MFM simulations with vibration.

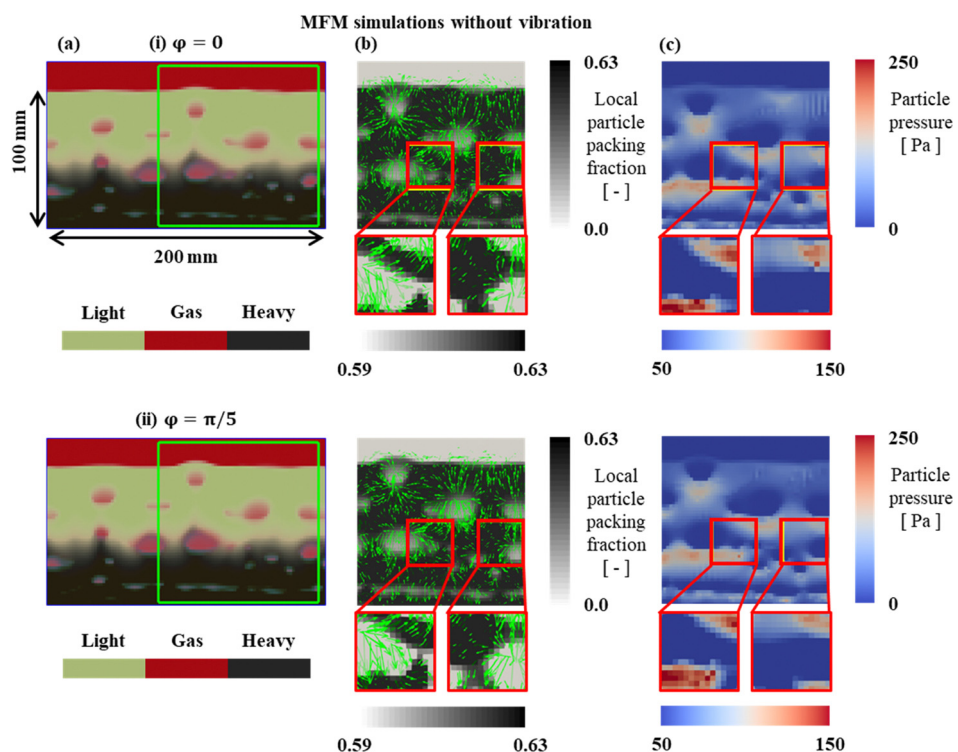


Fig. 22 (a) Heavy and light particle positions, (b) particle packing fraction and particle convection pattern and (c) particle pressure at two points in the vibration cycle in MFM simulations without vibration.

We further investigate why structured bubbling leads to greater mixing than unstructured bubbling (as seen in both experiments

and CFD-DEM simulations) by investigating CFD-DEM simulations in-depth. Fig. 23 shows CFD-DEM simulations (a) without

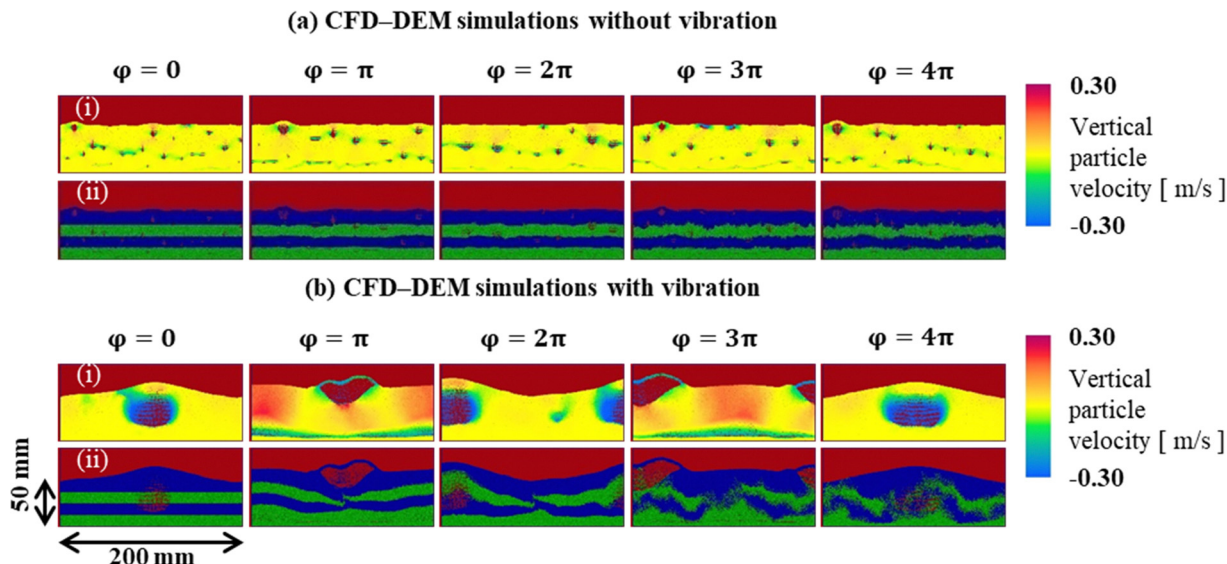


Fig. 23 (i) Vertical particle velocity and (ii) vertical mixing of tracer particles for CFD-DEM simulations (a) without vibration and (b) with vibration.

vibration and (b) with vibration over time through the course of two vibration cycles in the binary particle mixture after statistical steady state is reached. Simulations results show that there are somewhat fast upward and downward velocities surrounding small bubbles in the unstructured bubbling case without vibration (a), but overall the vertical particle velocities are close to zero. As such, in unstructured bubbling, there is not enough vertical motion of particles for inertia to overcome the buoyancy which keeps heavy particles at the bottom, and insignificant vertical mixing is observed over time. When vibration is used (b), large structured bubbles form and while bubbles rise through the center of the bed at the start of the vibration cycles, particles fall quickly through and to the sides of the bubbles. As bubbles break through the top of the bed at the middle of the vibration cycle, particles rise rapidly through the majority of the bed. As such, these dynamics of particles surrounding bubbles over the course of the vibration cycle create rapid up and down motion enabling inertia in the particles to overcome buoyant forces and allow heavy and light particles to mix vertically. Particle tracers (Fig. 23(b, ii)) show that most of the mixing occurs in the middle two vertical layers, while the top and bottom layers do not mix as much, which tracks with the fastest particle speeds seen in the vertical center of the bed. These tracer results explain why particle mixing is not complete in experiments and CFD-DEM simulations, but rather the top fourth of the bed is largely composed of light particles and the bottom fourth is largely composed of heavy particles.

**3.3.2 Discussion of differences between experiments and simulations.** As noted in the prior subsections, MFM simulations reproduced structured bubbling and a lack of structured bubbling with and without vibration, respectively, in a qualitative but not quantitative manner. MFM simulations failed to reproduce the key result that structured bubbling leads to mixing of the particles, which we have attributed in Section 3.3.4 to the inability to capture structured bubbling forming lower in the bed. The inaccuracies in predicting structured bubbling forming lower in the bed in MFM

can be attributed to aspects of the model which do not capture the full physics of the system, including: (i) the use of oscillating gravity to model vibration, (ii) the reduction in bed depth (8 mm experimentally to 4 mm in simulations) and (iii) inaccuracies in sub-models, such as particle–particle drag and solids rheology. In particular, the transition from fluid-like to solid-like behavior is key to the formation of structured bubbling, and thus more accurate modeling of solids rheology and how this rheology changes near boundaries is particularly important. These inaccuracies motivate future work to improve sub-models and boundary conditions within MFM.

CFD-DEM captured the bubbling and mixing dynamics quantitatively in the structured bubbling case with vibration and qualitatively in the unstructured bubbling case without vibration. The increased accuracy of CFD-DEM as compared to MFM can be attributed to the direct capturing of particle–particle and particle–wall contacts in CFD-DEM, thus avoiding the need to model solids rheology and solids–wall boundary conditions needed in MFM. The quantitative inaccuracies in CFD-DEM for predicting bubbling and resulting mixing dynamics in the unstructured bubbling case are most likely attributable to the drag law, since any drag law does not fully capture the no-slip boundary condition between particles and gas. Further, the drag law is key to predicting the particular size and rise velocity of bubbles in simulations,<sup>42</sup> since drag is the force that forms bubbles and causes them to rise in fluidized beds. These discrepancies may also form due to the fact that particles were modeled without a size distribution in the CFD-DEM simulations, and size distribution has been shown to be critical to bubble dynamics experimentally in fluidized beds.<sup>43</sup>

## 4. Conclusions and future work

Experimentally, we demonstrated that periodic, structured bubbling can form in binary mixtures of spherical granular



particles with similar  $U_{mf}$  values when subject to combined gas flow and vibration at specific conditions. The large bubbles formed by structured bubbling act to mix particles despite large differences in particle density, and mixing occurs regardless of the initial configuration of particles. When only gas flow is used, the bubbles formed are smaller and unstructured in nature, which leads to particles segregating, with light particles rising to the top. This ability to induce mixing with the use of vibration or segregation without the use of vibration provides the potential to use one mode when particle mixing is desired and another when segregation is desired for an engineering process, and thus these insights can be applied to industrial processes in future work. This study only investigated one particular set of gas flow and vibration conditions as well as one particular binary mixture of particles. Future studies could include a range of gas flow and vibration conditions as well as particles of different sizes, densities and shapes, including ternary and polydisperse mixtures, investigating their effects on bubble structuring and particle mixing.

Using computational modeling, CFD-DEM simulations provide predictions of structured bubbling and particle mixing which match experiments qualitatively and in some cases quantitatively. Detailed analysis of these simulations demonstrate that the structured bubbling forms due to particles below bubbles entering a solid-like state, causing a new row of bubbles to form at points horizontally in between the prior row of bubbles. Further, simulation analysis shows that the larger bubbles formed by structured bubbling cause a stronger inertial upwelling of particles in the wakes of bubbles, allowing these particles to overcome gravitational forces pulling them down to induce mixing. MFM simulations require the bed height to be increased in order to reproduce structured bubbling dynamics and do not predict mixing induced by structured bubbling. These results demonstrate the accuracy in predictions gained by extra computational cost using CFD-DEM as compared to MFM and indicate the importance of improving aspects of MFM simulations, such as solids phase rheology and solids-wall boundary conditions, in future work.

## Conflicts of interest

There are no conflicts to declare.

## Acknowledgements

This work was funded by the National Science Foundation Grant #2144763 and Office of Naval Research (ONR) grant N00014-22-1-2142.

## References

- 1 H. K. Pak and P. R. Behringer, *Nature*, 1994, **371**, 231–233.
- 2 P. B. Umbanhowar, F. Melo and H. L. Swinney, *Nature*, 1996, **382**, 793–796.
- 3 J. F. Davidson and D. Harrison, *Fluidised Particles*, Cambridge University Press, Cambridge, 1963.
- 4 L. de Martín, C. Ottevanger, J. R. van Ommen and M.-O. Coppens, *Phys. Rev. Fluids*, 2018, **3**, 034303.
- 5 C. Bizon, M. D. Shattuck, J. R. de Bruyn, J. B. Swift, W. D. McCormick and H. L. Swinney, *J. Stat. Phys.*, 1998, **93**, 449–465.
- 6 C. Bizon, M. D. Shattuck, J. B. Swift, W. D. McCormick and H. L. Swinney, *Phys. Rev. Lett.*, 1998, **80**, 57–60.
- 7 Q. Guo, C. Spitaler, J. M. Sanghishetty and C. M. Boyce, *Curr. Opin. Chem. Eng.*, 2023, **42**, 100977.
- 8 Q. Guo, Y. Zhang, A. Padash, K. Xi, T. M. Kovar and C. M. Boyce, *Proc. Natl. Acad. Sci. U. S. A.*, 2021, **118**, e2108647118.
- 9 Q. Guo, Y. Zhang, T. M. Kovar, K. Xi and C. M. Boyce, *Soft Matter*, 2022, **18**, 3323–3327.
- 10 Q. Guo, W. Da, R. Wu, Y. Zhang, J. Wei and C. M. Boyce, *Phys. Rev. E*, 2023, **107**, 034603.
- 11 T. M. Gernon, M. A. Gilbertson, R. S. J. Sparks and M. Field, *J. Volcanol. Geotherm. Res.*, 2008, **174**, 49–56.
- 12 D. Kadau, J. S. Andrade and H. J. Herrmann, *Granular Matter*, 2011, **13**, 219–223.
- 13 J. Adanez, A. Abad, F. Garcia-Labiano, P. Gayan and L. F. de Diego, *Prog. Energy Combust. Sci.*, 2012, **38**, 215–282.
- 14 I.-S. Han and C.-B. Chung, *Chem. Eng. Sci.*, 2001, **56**, 1951–1971.
- 15 A. Kiashemshaki, N. Mostoufi and R. Sotudeh-Gharebagh, *Chem. Eng. Sci.*, 2006, **61**, 3997–4006.
- 16 A. S. Mujumdar and K. Erdesz, *Drying Technol.*, 1988, **6**, 255–274.
- 17 B. Rambali, L. Baert and D. L. Massart, *Int. J. Pharm.*, 2001, **220**, 149–160.
- 18 J. M. Ottino and D. V. Khakhar, *Annu. Rev. Fluid Mech.*, 2000, **32**, 55–91.
- 19 M. O. Coppens and J. R. van Ommen, *Chem. Eng. J.*, 2003, **96**, 117–124.
- 20 C. S. Daw, C. E. A. Finney, M. Vasudevan, N. A. van Goor, K. Nguyen, D. D. Bruns, E. J. Kostelich, C. Grebogi, E. Ott and J. A. Yorke, *Phys. Rev. Lett.*, 1995, **75**, 2308–2311.
- 21 E. W. Merrow, Self-Organization and Chaos in a Fluidized Bed, 1984.
- 22 B. Formisani, G. D. Cristofaro and R. Girimonte, *Chem. Eng. Sci.*, 2001, **56**, 109–119.
- 23 N. Burtally, P. J. King and M. R. Swift, *Science*, 2002, **295**, 1877–1879.
- 24 S. R. Dahl and C. M. Hrenya, *Chem. Eng. Sci.*, 2005, **60**, 6658–6673.
- 25 A. Rosato, K. J. Strandburg, F. Prinz and R. H. Swendsen, *Phys. Rev. Lett.*, 1987, **58**, 1038–1040.
- 26 C. C. Lakshmanan and O. E. Potter, *Chem. Eng. Sci.*, 1990, **45**, 519–528.
- 27 Q. Guo and C. M. Boyce, *AIChE J.*, 2022, **68**, e17709.
- 28 L. A. Vandewalle, V. Francia, K. M. Van Geem, G. B. Marin and M.-O. Coppens, *Chem. Eng. J.*, 2022, **430**, 133063.
- 29 Y. Tsuji, T. Kawaguchi and T. Tanaka, *Powder Technol.*, 1993, **77**, 79–87.
- 30 P. A. Cundall and O. D. L. Strack, *Géotechnique*, 1979, **29**, 47–65.



31 T. B. Anderson and R. Jackson, *Ind. Eng. Chem. Fundam.*, 1967, **6**, 527–539.

32 D. Gidaspow, *Multiphase Flow and Fluidization: Continuum and Kinetic Theory Descriptions*, Academic Press, 1994.

33 C. M. Boyce, D. J. Holland, S. A. Scott and J. S. Dennis, *Ind. Eng. Chem. Res.*, 2015, **54**, 10684–10697.

34 J. M. Musser and J. E. Carney, *Theoretical Review of the MFIx Fluid and Two-Fluid Models*, NETL, 2020.

35 C. K. K. Lun, S. B. Savage, D. J. Jeffrey and N. Chepurniy, *J. Fluid Mech.*, 1984, **140**, 223–256.

36 R. Jackson, *Theory of Dispersed Multiphase Flow*, Elsevier, 1983, pp. 291–337.

37 J. Ding and D. Gidaspow, *AIChE J.*, 1990, **36**, 523–538.

38 D. Gera, M. Syamlal and T. J. O'Brien, *Int. J. Multiphase Flow*, 2004, **30**, 419–428.

39 P. C. Johnson and R. Jackson, *J. Fluid Mech.*, 1987, **176**, 67–93.

40 K. Pearson and O. M. F. E. Henrici, *Philos. Trans. R. Soc. London, Ser. A*, 1896, **187**, 253–318.

41 M. M. H. D. Arntz, W. K. den Otter, W. J. Briels, P. J. T. Bussmann, H. H. Beeftink and R. M. Boom, *AIChE J.*, 2008, **54**, 3133–3146.

42 D. Liu and B. van Wachem, *Powder Technol.*, 2019, **343**, 145–158.

43 J. W. Chew and R. A. Cocco, *Chem. Eng. J.*, 2021, **420**, 129880.